Traces of the $X(3960)$ state in the femtoscopic $D_s^+D_s^-$ correlations

Hao-Nan Liu
School of Physics, Beihang University, Beijing 102206, China

Zhi-Wei Liu[*]
Institute for Advanced Study in Nuclear Energy and Safety, College of Physics and Optoelectronic Engineering, Shenzhen University, Shenzhen 518060, China and Shenzhen Key Laboratory of Nuclear and Radiation Safety, Shenzhen 518060, China

Luciano Abreu[†]
Instituto de Física, Universidade Federal da Bahia, Campus Ondina, Salvador, Bahia 40170-115, Brazil

Li-Sheng Geng[‡]
Sino-French Carbon Neutrality Research Center, École Centrale de Pékin/School of General Engineering, Beihang University, Beijing 100191, China, School of Physics, Beihang University, Beijing 102206, China, Peng Huanwu Collaborative Center for Research and Education, Beihang University, Beijing 100191, China, Beijing Key Laboratory of Advanced Nuclear Materials and Physics, Beihang University, Beijing 102206, China, and Southern Center for Nuclear-Science Theory (SCNT), Institute of Modern Physics, Chinese Academy of Sciences, Huizhou 516000, China

(Received 26 November 2025; accepted 8 May 2026; published 4 June 2026)

The femtoscopic $D_s^+D_s^-$ correlations are investigated to predict the signature of the not-yet-established $X(3960)$ state reported by the LHCb Collaboration in three scenarios: resonant, virtual, or bound. In the last two scenarios, it might also be identified as the state $X(3930)$. The formalism employed to generate this structure dynamically is based on the Bethe-Salpeter equation with a general S-wave potential. We investigate how the relevant properties and observables characterizing this state—such as the pole position, scattering length, and effective range—might be affected by variations in the model parameters. The amplitudes encoding the distinct interpretations of the $X(3960)$ state are then used as input to calculate the femtoscopic correlation function of the $D_s^+D_s^-$ pair, which is analyzed and discussed.

DOI: 10.1103/l3xr-phbj

I. INTRODUCTION

Recently, the LHCb Collaboration reported the observation of the so-called $X(3960)$ state in the $D_s^+D_s^-$ invariant-mass spectrum of $B^+ \to D_s^+D_s^-K^+$ decays [1]. The analysis favored $J^{PC} = 0^{++}$ quantum numbers, with the following fitted mass and width:

$$m_{X(3960)} = 3956 \pm 5 \pm 10 \text{ MeV},$$
$$\Gamma_{X(3960)} = 43 \pm 13 \pm 8 \text{ MeV}. \quad (1)$$

It appears in addition to another 0^{++} state denoted as $X(3930)$, observed by LHCb in the D^+D^- invariant-mass distribution of the $B^+ \to D^+D^-K^+$ decay [2,3], with the following measured observables:

$$m_{X(3930)} = 3924 \pm 2 \text{ MeV}, \qquad \Gamma_{X(3930)} = 17 \pm 5 \text{ MeV}. \quad (2)$$

These LHCb measurements [2,3] are consistent with earlier observations by the Belle [4,5] and *BABAR* [6,7] Collaborations of a similar state, referred to as $X(3915)$.

The proximity of both $X(3930)$ and $X(3960)$ to the $D_s^+D_s^-$ threshold ($M^{\text{thr}}_{D_s^+D_s^-} = 3936.7$ MeV) has given rise to intense debate about their possible molecular interpretations, particularly since their masses deviate significantly from

[*]Contact author: liuzhw@szu.edu.cn
[†]Contact author: luciano.abreu@ufba.br
[‡]Contact author: lisheng.geng@buaa.edu.cn

Published by the American Physical Society under the terms of the Creative Commons Attribution 4.0 International license. Further distribution of this work must maintain attribution to the author(s) and the published article's title, journal citation, and DOI. Funded by SCOAP³.

quark model predictions for the conventional $\chi_{c0}(3P)$ charmonia [8,9]. Equally important is the controversy concerning whether they represent distinct states or different manifestations of the same structure. As discussed in Refs. [10–13], the near-threshold enhancement in $D_s^+D_s^-$ does not necessarily imply a new resonance. In Ref. [10], a coupled-channel analysis of $D\bar{D}$ and $D_s\bar{D}_s$ systems revealed two poles: one below the $D\bar{D}$ threshold, identified as $X(3700)$ (previously predicted in other works [14–19]) and another below the $D_s^+D_s^-$ threshold corresponding to $X(3930)$, which couples more strongly to $D_s\bar{D}_s$ than to $D\bar{D}$. These couplings successfully reproduce both the D^+D^- peak in $B^+ \to D^+D^-K^+$ decays and the $D_s^+D_s^-$ threshold enhancement in $B^+ \to D_s^+D_s^-K^+$ decays observed by LHCb. In this picture, the $X(3960)$ signal arises from a kinematic threshold enhancement driven by the $X(3930)$ state, interpreted as a molecular state dominated by $D_s\bar{D}_s$ components near threshold. Complementary support comes from Ref. [13], which employed the same approach to analyze the $J/\psi\omega$ mass distribution in $B^- \to K^-J/\psi\omega$ decays, with the final state arising from rescattering of $D\bar{D}$ and $D_s\bar{D}_s$ intermediate components.

However, the precise nature of the pole associated with $X(3930)$ remains ambiguous. Reference [12] utilized an effective field theory based on heavy quark spin symmetry and concluded that the LHCb data can be equally well described by different pole structures: either a bound or virtual state below the $D_s\bar{D}_s$ threshold. The analysis suggested that current experimental data cannot definitively discriminate between these scenarios. Meanwhile, the LHCb amplitude analysis [1] also allows for a conventional resonant-state interpretation. In addition, the recent lattice calculations find no support for a bound $D_s\bar{D}_s$ state and instead point to a single 0^{++} resonance [20].

Other approaches have been proposed to describe the $D_s^+D_s^-$ enhancement. These include molecular interpretations using QCD sum rules [21,22], boson exchange models with coupled channels that find resonant states [23], and tetraquark interpretations involving scalar diquark-antidiquark configurations within QCD sum rules [24] or chromomagnetic interaction models [25]. The $X(3915)$ and $X(3960)$ have also been proposed as four-quark states within an extended recoupling model [26]. Additionally, the production rate of $B^+ \to X(3960)K^+$ has been calculated assuming $X(3960)$ to be a molecular $D_s^+D_s^-$ state using the compositeness condition [27].

The persistent ambiguity in interpreting the near-threshold $D_s^+D_s^-$ enhancement highlights the need for additional experimental and theoretical studies employing observables that can distinguish among the different interpretations. In this regard, femtoscopic correlation analyses offer a promising approach [28–31]. By measuring two-particle correlations in high-multiplicity collisions, one can extract low-energy interaction parameters such as the scattering length a_0 and effective range r_0, which are sensitive to the underlying structure of hadronic states [19,32–42]. Recent advances in heavy-flavor femtoscopy at the LHC suggest that such measurements are becoming feasible [43,44]. A combined analysis of line shapes and femtoscopic correlations could provide complementary constraints, enhancing our understanding of exotic structures [30,37].

Thus, in this work, we employ femtoscopic correlations to discriminate between three possible scenarios for the nature of the $X(3960)$ state: a near-threshold resonance, a virtual state, or a bound state. Following the approach of Ref. [37], we utilize the Bethe-Salpeter formalism to parametrize the strong $D_s^+D_s^-$ interaction, as detailed in Sec. II. The resulting scattering amplitude is then combined with the Coulomb interaction to construct the complete amplitude used in the femtoscopic correlation function (CF), which is presented and analyzed in Sec. III. We demonstrate that low-momentum correlation functions across different collision systems (e.g., pp, pA, and AA) exhibit distinctive patterns in each of the three scenarios, thereby providing an alternative tool for resolving current interpretive ambiguities. Finally, a summary of our main findings and conclusions is presented in Sec. IV.

II. THE STRONG INTERACTION CONTRIBUTION TO THE TRANSITION AMPLITUDE

A. Formalism

We start by introducing the strong contribution to the $D_s^+D_s^-$ amplitude, obtained via the Bethe-Salpeter formalism and used as input to the $D_s^+D_s^-$ CF. Here we benefit from the analyses done in Refs. [11,37] exploring distinct configurations for exotic states (see also Refs. [45,46]). In particular, Ref. [11] employed a contact potential from a nonrelativistic effective field theory considering heavy quark spin and light-flavor SU(3) symmetries. The low-energy constants (LECs) have been determined by fitting the line shapes of the $D_s^+D_s^-$ invariant-mass distribution of the $B^+ \to D_s^+D_s^-K^+$ reaction to the LHCb data reported in Ref. [1]. The conclusion of Ref. [11] was that the $X(3960)$ state might be compatible with either a bound or virtual state in the $D_s^+D_s^-$ channel. In turn, in the study of the possible femtoscopic signatures of the $Z_c(3900)/Z_{cs}(3985)$ states, Ref. [37] used a general S-wave potential up to the next-to-leading order in momentum expansion for the $D^0D^{*-}/D^0D_s^{*-}$ systems. Accordingly, the LECs have been determined by exploring the scenarios of bound, virtual, and resonant states. In the latter case, the poles reported by the Particle Data Group have been employed, and the former two have been fine-tuned to obtain line shapes similar to those of the resonant state. For the determination of the strong $D_s^+D_s^-$ amplitude, we adopt the potential and fit the LECs similar to the framework of [37].

We define the S-wave projected strong potential for the process $D_s^+D_s^- \to D_s^+D_s^-$ as[1]

[1]Note that the Coulomb interaction is neglected here and will only be considered in predicting the corresponding femtoscopy correlation function in Sec. III.

$$V^{(\mathrm{S})} = a + bk^2, \tag{3}$$

where $k = \lambda^{1/2}(s, m_{D_s}^2, m_{D_s}^2)/(2\sqrt{s})$ is the relative momentum of the meson pair, with $\lambda(x, y, z)$ being the Källen function, m_{D_s} the mass of the D_s^+, D_s^- mesons, and s the squared center-of-mass (CM) energy; and a, b are the free parameters (i.e., LECs) to be determined.

The unitarized scattering amplitude matrix of the strong interaction $T^{(\mathrm{S})}$ is then obtained by solving the Bethe-Salpeter equation,

$$T^{(\mathrm{S})} = [1 - V^{(\mathrm{S})}G]^{-1}V^{(\mathrm{S})}, \tag{4}$$

where G is the loop function for two intermediate mesons in a given channel, which in the cutoff regularization scheme can be written as

$$G(\sqrt{s}) = \int_0^{q_{\max}} \frac{q^2 \mathrm{d}q}{2\pi^2} \frac{1}{4\omega_{D_s}^2(q)} \frac{1}{\sqrt{s} - 2\omega_{D_s}(q) + i\varepsilon}, \tag{5}$$

with $\omega_{D_s}(q) = \sqrt{q^2 + m_{D_s}^2}$, and $q_{\max}$ being the cutoff chosen within the range 0.5–1.0 GeV.

We identify virtual, bound, and resonant states through poles of the $T^{(\mathrm{S})}$-matrix in the Riemann sheets of the $\sqrt{s}$ plane [37]. Virtual and bound states correspond to poles on the real axis below threshold in the second and first Riemann sheets, respectively; while resonances appear as complex poles in the second Riemann sheet, with their mass and half-width being given by the real and imaginary parts of the pole position. The second Riemann sheet loop function $G^{(\mathrm{II})}$ is obtained via analytic continuation: $G^{(\mathrm{II})} = G + 2i\rho$, where $\rho = k/(8\pi\sqrt{s})$ is the phase-space factor.

We also calculate two key low-energy scattering observables defined by the effective range expansion (ERE) [37,45–48]: the scattering length a_0 and the effective range r_0. Using the relation between the $T^{(\mathrm{S})}$-matrix and phase shift δ_0, $T^{(\mathrm{S})} \propto (k\cot\delta_0 - ik)^{-1}$, the expansion can be written as

$$-8\pi\sqrt{s}T^{(\mathrm{S})-1} + ik = -\frac{1}{a_0} + \frac{1}{2}r_0k^2 + \mathcal{O}(k^4). \tag{6}$$

From this relation, a_0 and r_0 are given by

$$a_0 = \left.\frac{T^{(\mathrm{S})}}{8\pi\sqrt{s}}\right|_{s=s_{\mathrm{thr}}},$$
$$r_0 = \frac{\partial^2}{\partial k^2}(-8\pi\sqrt{s}T^{(\mathrm{S})-1} + ik)|_{s=s_{\mathrm{thr}}}. \tag{7}$$

Here, s_{thr} is the squared CM energy at the channel's threshold. We note that the $+ik$ term in Eqs. (6) and (7) is essential for satisfying the unitarity condition required by the ERE. It ensures that any linear-k imaginary contributions arising from the loop function G cancel in the expansion, leaving a real result. When the derivative is taken at threshold, as in the definition (7) of r_0, the loop function G and its derivative are evaluated on the physical sheet. For bound states, this procedure is straightforward. For virtual states and resonances, although the pole resides on the unphysical sheet, the calculation of r_0 remains on the physical sheet at threshold, where G is real because the phase-space factor vanishes. Therefore, within our single-channel formalism, the effective range is real.

To determine the LECs, we employ the $D_s^+D_s^-$ invariant-mass distribution of the $B^+ \to D_s^+D_s^-K^+$ reaction, which is given by [10,11]

$$\frac{\mathrm{d}\Gamma}{\mathrm{d}M_{\mathrm{inv}}} = \frac{1}{(2\pi)^3}\frac{1}{4m_B^2}p_{K^+}\tilde{p}_{D_s}|\tilde{T}|^2, \tag{8}$$

where M_{inv} is the invariant mass of the $D_s^+D_s^-$ system; $p_{K^+} = \lambda^{1/2}(m_{B^+}^2, m_{K^+}^2, M_{\mathrm{inv}}^2)/2m_{B^+}$ and $\tilde{p}_{D_s} = \lambda^{1/2}(M_{\mathrm{inv}}^2, m_{D_s^+}^2, m_{D_s^-}^2)/2M_{\mathrm{inv}}$ are, respectively, the K^+ and D_s momenta; and $\tilde{T}$ is the amplitude for the $B^+ \to D_s^+D_s^-K^+$ transition.

The analytical expression for $\tilde{T}$ can be obtained as follows [10,11]. At the quark level, these B-decays proceed via a Cabibbo-suppressed internal W-emission: $\bar{b}(\to \bar{c}W^+ \to \bar{c}c\bar{s})u \to \bar{c}c(\bar{s}u)$. After hadronization of the $c\bar{c}$ pair, only the $D_s^+D_s^-$ channel remains. At the hadron

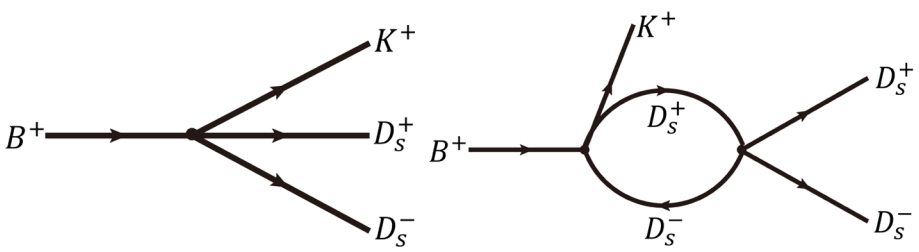

FIG. 1. Mechanisms contributing to the $B^+ \to D_s^+D_s^-K^+$ reaction. (a) Tree-level contribution. (b) Rescattering contribution.

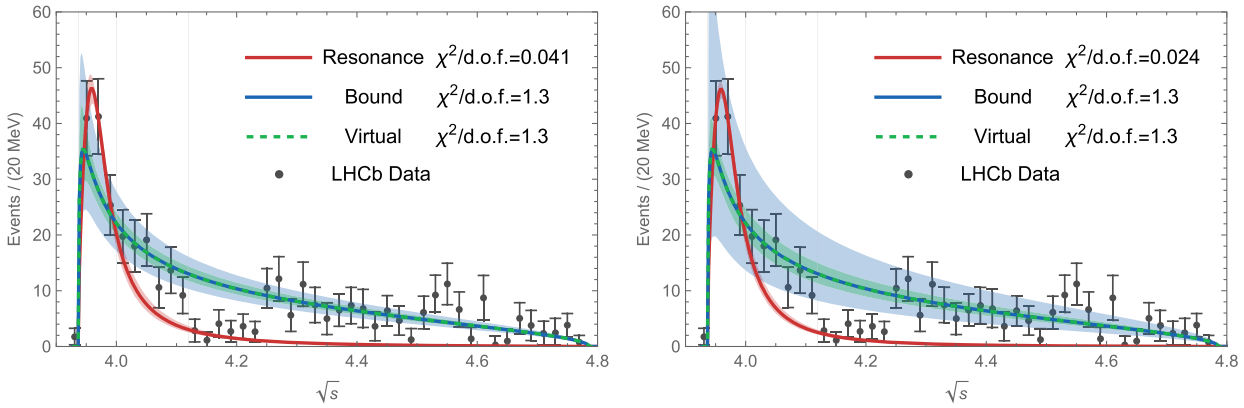

FIG. 2. Differential distributions of the $B^+ \to D_s^+ D_s^- K^+$ decay taking (a) $q_{\max} = 1.0$ GeV and (b) $q_{\max} = 0.5$ GeV. The shaded areas represent the uncertainties in the LECs displayed in Table I for the different scenarios. The experimental data are taken from Ref. [1]. The first vertical gray line corresponds to the $D_s^+ D_s^-$ threshold.

level, the production mechanisms considered for $B^+ \to D_s^+ D_s^- K^+$ are the tree-level and one-loop contributions, as depicted in Fig. 1. Consequently, the effects of the state under investigation are produced through the interaction of the intermediate $D_s^+ D_s^-$ pair in the rescattering contribution.

So, the amplitude for the diagrams in Fig. 1 is given by

$$\tilde{T}(M_{\rm inv}) = C[1 + G(M_{\rm inv}) T^{(\rm S)}(M_{\rm inv})], \tag{9}$$

where C is an overall constant encoding effectively the information of the weak vertex, $G(M_{\rm inv})$ is the two-meson loop function given in Eq. (5), and $T^{(\rm S)}(M_{\rm inv})$ is the unitarized scattering amplitude matrix given in Eq. (4).

B. Fitting results

Using Eqs. (9) and (8), we fit the LECs a and b of the potential $V^{(\rm S)}$ to reproduce the LHCb data [1] via the least-squares minimization. In the bound- and virtual-state scenarios, the fit considers the first ten data points in the CM energy region from 3.92 to 4.12 GeV (data before the third vertical gray line), as in Ref. [11]. In the resonant-state scenario, only the first four data points (those before the second vertical gray line) are used. These restricted ranges are chosen because our model focuses on the region near the $D_s^+ D_s^-$ threshold and excludes other irrelevant effects or states at higher energies. In the resonant-state scenario, the invariant-mass spectrum is expected to feature a narrow, Breit-Wigner-like peak (as shown in Fig. 2 of Ref. [1]), whose essential characteristics are encapsulated within the first four data points. Fitting exclusively to these points thus results in a small value of χ^2 per degree of freedom (χ^2/d.o.f.) value, which we consider sufficient for a qualitative discussion of the resonant interpretation.

Figure 2 shows the fitted differential mass distributions for a cutoff parameter $q_{\max} = 1.0$ GeV in the bound, virtual, and resonant scenarios. All three cases produce line shapes compatible with the data, with those for bound

TABLE I. Relevant quantities obtained from the fits to the LHCb data in Ref. [1]: mass and width of the pole position, the LECs a, b, the scattering length a_0, and the effective range r_0 and the overall constant C. The $D_s^+ D_s^-$ threshold is 3936.7 MeV.

$q_{\max} = 1.0$ GeV							
Scenario	M (MeV)	Γ (MeV)	a	$b(10^{-6}\ \text{MeV}^{-2})$	C	a_0 (fm)	r_0 (fm)
Resonance	$3948.79^{+2.44}_{-3.33}$	$60.04^{+10.83}_{-8.72}$	-106.67 ± 3.53	-629.75 ± 73.62	811.98 ± 14.07	$-0.63^{+0.06}_{-0.07}$	$-1.86^{+0.28}_{-0.30}$
Bound	$3928.27^{+3.55}_{-4.07}$	0	-202.61 ± 11.22	0.00	947.82 ± 91.89	$1.60^{+0.48}_{-0.28}$	$0.28^{+0.001}_{-0.001}$
Virtual	$3928.28^{+3.31}_{-4.44}$	0	-132.57 ± 5.67	0.00	673.81 ± 30.47	$-1.47^{+0.29}_{-0.43}$	$0.29^{+0.002}_{-0.002}$
$q_{\max} = 0.5$ GeV							
Scenario	M (MeV)	Γ (MeV)	a	$b(10^{-6}\ \text{MeV}^{-2})$	C	a_0 (fm)	r_0 (fm)
Resonance	$3949.43^{+2.04}_{-2.60}$	$63.75^{+8.30}_{-6.98}$	-136.79 ± 8.17	-1431.33 ± 145.39	1372.73 ± 18.54	$-0.48^{+0.05}_{-0.05}$	$-2.45^{+0.44}_{-0.51}$
Bound	$3928.27^{+3.85}_{-3.73}$	0	-517.19 ± 73.08	0.00	2419.39 ± 429.91	$1.60^{+0.53}_{-0.26}$	$0.51^{+0.002}_{-0.001}$
Virtual	$3928.28^{+3.24}_{-4.57}$	0	-220.19 ± 15.64	0.00	1119.20 ± 55.47	$-1.47^{+0.30}_{-0.42}$	$0.53^{+0.002}_{-0.002}$

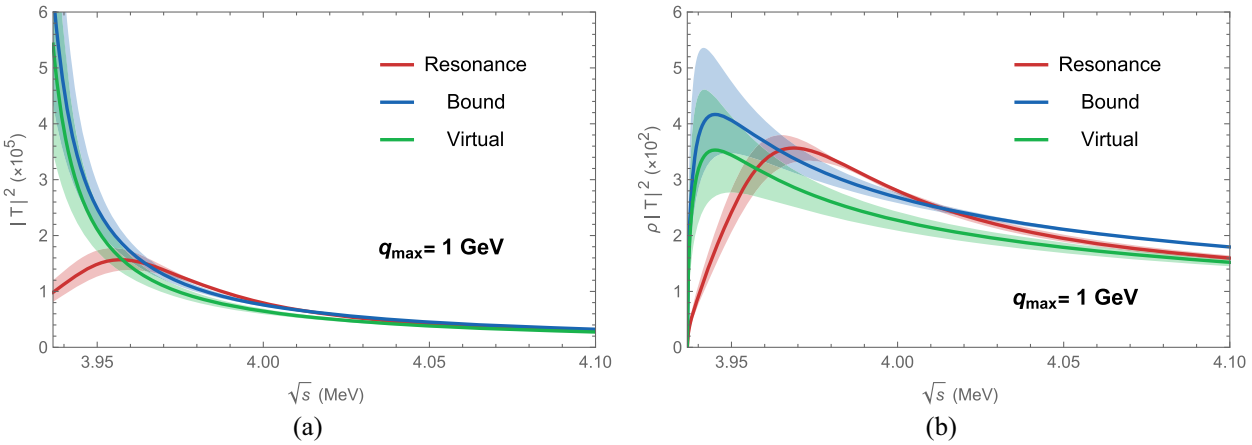

FIG. 3. (a) Modulus square of the amplitude of the $D_s^+D_s^- \to D_s^+D_s^-$ channel as a function of the CM energy. (b) Modulus square of the amplitude times the phase-space factor of the $D_s^+D_s^- \to D_s^+D_s^-$ channel as a function of the CM energy. The shaded areas represent the uncertainties in the LECs displayed in Table I for the different scenarios.

and virtual states being practically indistinguishable. Table I provides the fitted values of a and b, along with the resulting pole positions, scattering lengths a_0, and effective ranges r_0 in the three scenarios. For completeness, we also include results for $q_{\max} = 0.5$ GeV.

The pole positions for the virtual and bound state interpretations are consistent with those obtained in Refs. [3,11] within uncertainties, which are associated with the $X(3930)$ state. The resonant-state scenario yields a pole position consistent with that reported by the LHCb Collaboration [1], where a new state, referred to as $X(3960)$, is claimed.

We emphasize that the parameter C in Eq. (9) only appears in the invariant-mass distribution and does not affect the scattering amplitude or correlation function. The difference between bound- and virtual-state scenarios in the error band widths in Fig. 2 arises not only from the uncertainty of a listed in Table I, but also from that of C. As shown in Table I, the relative uncertainty of C is significantly larger for the bound-state scenario than for the virtual-state scenario, leading to a broader uncertainty band for the bound-state case in Fig. 2.

This also explains why, in Figs. 2(a) and 2(b), the uncertainty bands for the virtual-state scenario are comparable, while the bound-state band is wider in Fig. 2(b) than in Fig. 2(a). For the virtual-state scenario, the relative uncertainty of C is similar at $q_{\max} = 0.5$ and 1 GeV. For the bound-state scenario, it is notably larger at 0.5 GeV, resulting in the broader band in Fig. 2(b).

In other figures (e.g., Figs. 3–5), only the uncertainty of a (and b for the resonant-state scenario) is propagated, as C does not enter the T-matrix or correlation function. Hence, the uncertainty bands in those figures are comparable between bound- and virtual-state scenarios.

For completeness, Fig. 3 shows the squared amplitude and the squared amplitude times the phase-space factor for the $D_s^+D_s^- \to D_s^+D_s^-$ channel as a function of the CM energy, for a cutoff parameter $q_{\max} = 1.0$ GeV. The inherent kinematic suppression due to the phase-space factor in the near-threshold region makes it difficult to distinguish among the different configurations in the invariant-mass spectrum.

It is most important to emphasize that all three scenarios can fairly reproduce the low-energy experimental data within current uncertainties. This demonstrates that the invariant-mass distribution alone is insufficient to distinguish between these interpretations. Additional observables are therefore necessary to discriminate among the different configurations and clarify this ambiguity.

We now examine how these scenarios manifest in femtoscopic correlation functions.

III. CORRELATION FUNCTIONS

A. Formalism

The CF for two-particle systems is defined as the ratio of the probability of measuring the two-particle state to the product of the probabilities of measuring each particle [49]. According to the Koonin-Pratt approach, after some manipulations, the CF can be given by the following formula [28,50,51]:

$$C(k) = \int \mathrm{d}^3 r S_{12}(\boldsymbol{r}) |\Psi(\boldsymbol{k};\boldsymbol{r})|^2, \tag{10}$$

where $\boldsymbol{k}$ is the relative momentum in the CM frame of the pair; $\boldsymbol{r}$ is the relative distance between the two particles; $\Psi(\boldsymbol{k};\boldsymbol{r})$ is the relative two-particle wave function carrying information of final-state interactions; and $S_{12}(\boldsymbol{r})$ is the source function encoding the particle-emitting source.

In the present work, we adopt the source function in its usual static Gaussian profile normalized to unity, i.e., [28,29]

$$S_{12}(\boldsymbol{r}) = \frac{1}{(4\pi)^{\frac{3}{2}} R^3} \exp\left(-\frac{r^2}{4R^2}\right), \tag{11}$$

where R is the source size, treated as a free parameter which is chosen in such a way to reproduce the characteristic scale of the particle-emitting source in different collision systems: smaller values (e.g., $R \propto 1$ fm) correspond to high-multiplicity pp collisions, while larger values (up to several femtometers) are typical for central AA collisions. We remark that the choice of a Gaussian source is motivated by its simplicity and by the expectation that feed-down contributions from strong decays are minimal for charm mesons, making it a reasonable approximation in this exploratory study. In future experimental studies, the source size can be anchored to proton-proton correlation data by measuring the m_{T} of the $D_s^+ D_s^-$ pair, thereby reducing systematic uncertainties.

A realistic treatment of the $|D_s^+ D_s^-\rangle$ system must include the Coulomb interaction due to its significant role [52]. We therefore employ a relative wave function that incorporates both the S-wave strong interaction and the Coulomb potential [53],

$$\Psi(\boldsymbol{k};\boldsymbol{r}) = \Phi^{(\mathrm{C})}(\boldsymbol{k};\boldsymbol{r}) - \Phi_0^{(\mathrm{C})}(k,r) + \psi_0(k,r), \quad (12)$$

where $\Phi^{(\mathrm{C})}(\boldsymbol{k};\boldsymbol{r})$ is the complete Coulomb wave function [54], $\Phi_0^{(\mathrm{C})}(k,r)$ is its S-wave component, and $\psi_0(k,r)$ contains the full strong interaction in the presence of the Coulomb potential.

Using the wave function in Eq. (12) and assuming a spherically symmetric source function from Eq. (11), the Koonin-Pratt formula in Eq. (10) becomes [33,39,45,47,52,55,56]

$$C(k) = \int \mathrm{d}^3\boldsymbol{r} S_{12}(\boldsymbol{r}) |\Phi^{(\mathrm{C})}(\boldsymbol{k};\boldsymbol{r})|^2 + \int_0^\infty 4\pi r^2 \mathrm{d}r S_{12}(\boldsymbol{r}) (|\psi_0(k,r)|^2 - |\Phi_0^{(\mathrm{C})}(k,r)|^2). \quad (13)$$

Following the notation of Refs. [19,57], the complete Coulomb wave function is given by [54]

$$\Phi^{(\mathrm{C})}(k;\boldsymbol{r},z) = e^{-\pi\gamma/2}\Gamma(1+i\gamma) e^{ikz}\, {}_1F_1(-i\gamma;1;ik(r-z)). \quad (14)$$

Here, $\Gamma(z)$ is the Euler gamma function, ${}_1F_1(a;b;z)$ is the confluent hypergeometric function (Kummer's function), and γ is the Sommerfeld parameter,

$$\gamma = Z_1 Z_2 \frac{\mu\alpha}{k}, \quad (15)$$

with $Z_1 Z_2$ being the product of the charges, α is the fine-structure constant, and μ is the reduced mass of the hadron pair.

The S-wave function $\psi_0(k,r)$ is obtained from the Lippmann-Schwinger equation $|\psi\rangle = |\phi\rangle + GT|\phi\rangle$, where $|\phi\rangle$ is the free wave function [34,53,57],

$$\psi_0(k,r) = j_0(kr) + \int_0^{q_{\max}} \frac{q^2 \mathrm{d}q}{2\pi^2} \frac{1}{4\omega_{D_s}^2(q)} \frac{T(k,q;s) j_0(qr)}{\sqrt{s} - 2\omega_{D_s}(q) + i\varepsilon}. \quad (16)$$

Here, $j_\nu(x)$ is the spherical Bessel function of order ν, and $T(k,q;s)$ is the S-wave scattering amplitude for the charged meson pair including both strong and Coulomb contributions.

Ideally, the amplitude $T(k,q;s)$ should be obtained by simultaneously unitarizing the combined strong and Coulomb amplitudes. Since the Coulomb contribution depends on the meson momenta in both initial and final states, this requires solving the full off-shell Bethe-Salpeter equation. However, following the analysis in Ref. [53], the momentum integral in Eq. (16) is calculated with the Coulomb amplitude up to first order in the Bethe-Salpeter equation combined with the on-shell strong amplitude studied in the previous section. Given the exploratory nature of this study, this approximation has the practical advantage of leaving the fitted strong amplitude unchanged.

Explicitly, the full scattering amplitude is decomposed as

$$T(p,p';s) = T^{(\mathrm{S})}(\sqrt{s}) + T^{(\mathrm{C})}(p,p';s), \quad (17)$$

where $T^{(\mathrm{S})}(\sqrt{s})$ is the unitarized strong amplitude from Eq. (4) and $T^{(\mathrm{C})}(p,p';s)$ is the Coulomb amplitude in the Born approximation,

$$T^{(\mathrm{C})}(p,p';s) = V_0^{(\mathrm{C,rel})}(p,p';s). \quad (18)$$

To obtain the Coulomb contribution $V_0^{(\mathrm{C,rel})}(p,p';s)$, we begin with the Fourier transform of the potential $V^{(C)} = \epsilon\alpha/r$, where $\epsilon = +1(-1)$ for identical (opposite) charged particles, into momentum space,

$$V_{\mathrm{total}}^{(\mathrm{C})}(|\boldsymbol{p}' - \boldsymbol{p}|) = \int_0^{R_C} \mathrm{d}^3 r e^{i(\boldsymbol{p}'-\boldsymbol{p})\cdot\boldsymbol{r}} \frac{\epsilon\alpha}{r} = \frac{4\pi\epsilon\alpha}{|\boldsymbol{p}'-\boldsymbol{p}|^2}(1 - \cos(|\boldsymbol{p}'-\boldsymbol{p}|R_C)), \quad (19)$$

where only the short-range Coulomb interaction ($r < R_C$) is considered to avoid divergences in the integrals. The long-range behavior will be accounted for through the asymptotic wave functions.

The S-wave component of this potential is obtained by projecting it onto the partial wave,

$$V_0^{(\mathrm{C})}(p,p') = \frac{1}{2}\int_{-1}^{1} \mathrm{d}(\cos\theta_{\boldsymbol{App}'}) V_{\mathrm{total}}^{(\mathrm{C})}(|\boldsymbol{p}'-\boldsymbol{p}|) \quad (20)$$

$$= \frac{2\pi\epsilon\alpha}{pp'}\left\{\mathrm{Ci}[|p'-p|R_C] - \mathrm{Ci}[|p'+p|R_C] + \ln\left(\frac{p'+p}{|p'-p|}\right)\right\}, \quad (21)$$

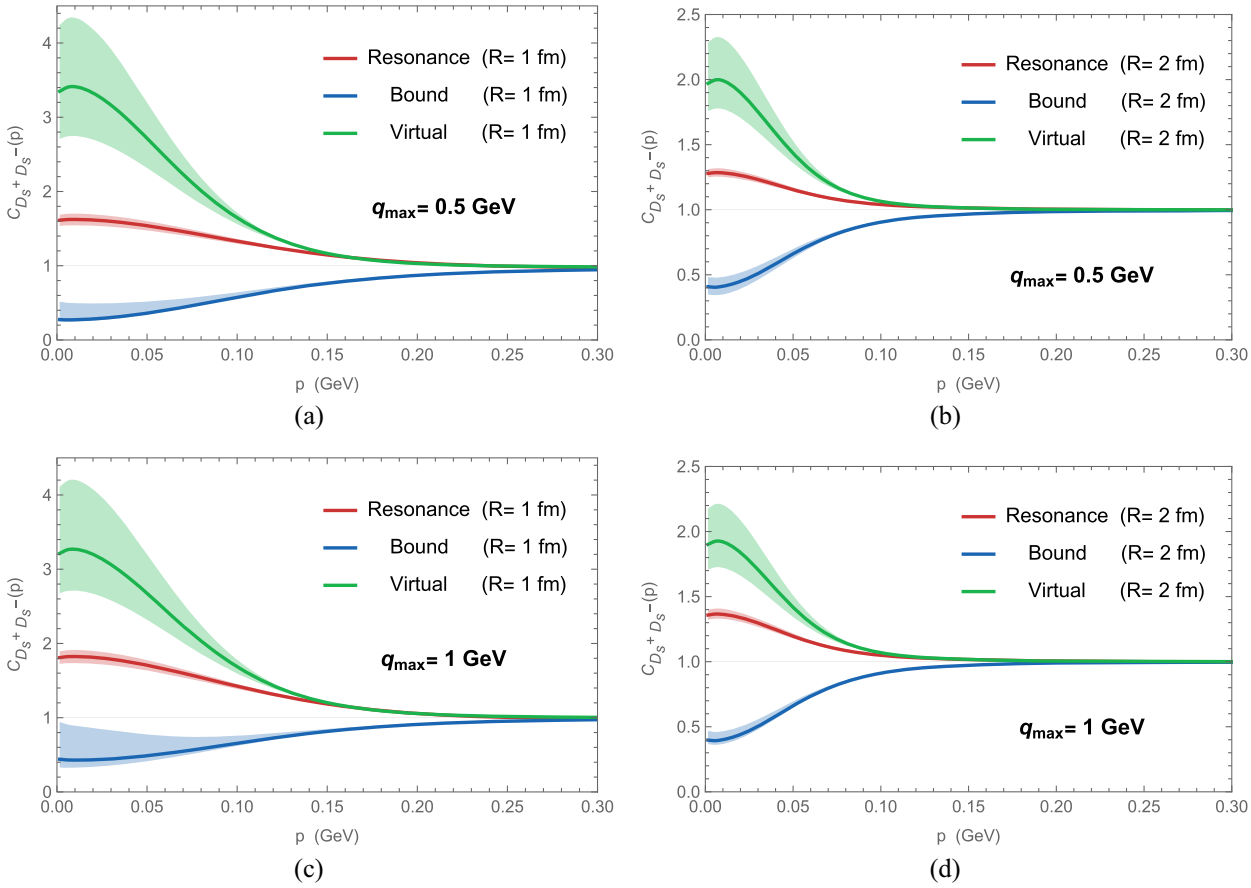

FIG. 4. (a)–(d) The pure strong contribution of the $D_s^+ D_s^-$ CF as a function of the CM relative momentum k, taking different values of the size parameter R in three scenarios. The shaded areas represent the uncertainties in the LECs displayed in Table I for the different scenarios.

where $\mathrm{Ci}[x] = \int_x^\infty \mathrm{d}t(\cos t)/t$ is the cosine integral function. We have tested various values of R_C and find that our results stabilize at $R_C = 4$ fm, which we therefore adopt in all subsequent calculations.

To consistently incorporate the Coulomb interaction within the relativistic Bethe-Salpeter equation, the S-wave Coulomb potential must be modified with relativistic kinematic factors [53,57],

$$V_0^{(\mathrm{C,rel})}(p,p';s) = 2\omega_{D_s}(p)\sqrt{\xi(p;s)}V_0^{(\mathrm{C})}(p,p') \times \sqrt{\xi(p';s)}2\omega_{D_s}(p'), \tag{22}$$

where the kinematic factors $\xi(p;s)$ are given by

$$\xi(p;s) = 2\mu\frac{\sqrt{s}-2\omega_{D_s}(p)}{\frac{\lambda(s,m_1^2,m_2^2)}{4s}-p^2}, \tag{23}$$

with $\mu = m_{D_s}/2$ being the reduced mass.

B. Results and discussions

Figure 4 shows the pure strong $D_s^+ D_s^-$ CF as a function of the CM relative momentum k for different values of the parameter R in three scenarios. This contribution is calculated by replacing the $\Phi^{(\mathrm{C})}$ and $\Phi_0^{(\mathrm{C})}$ with $e^{ik\cdot r}$ and j_0 in Eq. (13) and using the scattering amplitude $T(k,q;s) = T^{(\mathrm{S})}(s)$ in Eq. (16), which contains only the unitarized strong interaction. In the low-momentum region, the pure strong $D_s^+ D_s^-$ CF exhibits distinct and typical behavior for each configuration. Specifically, compared to unity, the virtual- and bound-state scenarios produce, respectively, enhancements and suppressions in the low-momentum correlations, while the resonant configuration yields a moderate enhancement. This distinction is most pronounced for smaller values of the source size parameter R and becomes less significant as R increases. These findings are qualitatively consistent with those obtained in Ref. [37] in investigating femtoscopic signatures for the $Z_c(3900)/Z_{cs}(3985)$ states in the $D^0 D^{*-}/D^0 D_s^{*-}$ systems. However, a difference can be noted in the resonant interpretation. Because of the larger width given in Table I, the $D_s^+ D_s^-$ CF in Fig. 4 does not exhibit a

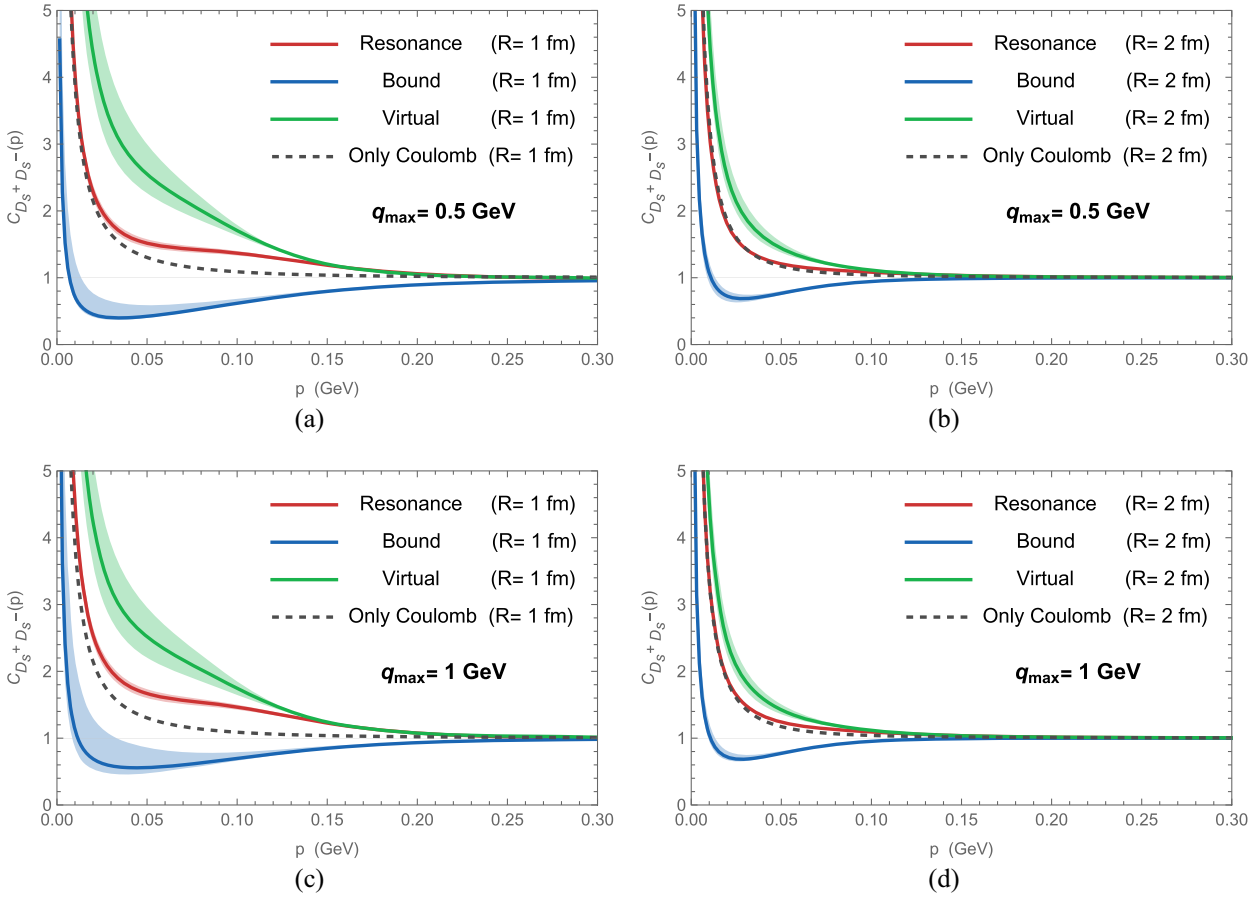

FIG. 5. (a)–(d) The total $D_s^+ D_s^-$ CF as a function of the CM relative momentum k, taking different values of the size parameter R in three scenarios. The shaded areas represent the uncertainties in the LECs displayed in Table I for the different scenarios.

pronounced dip in the intermediate-momentum region. Specifically, in the momentum region slightly above the resonance pole, i.e., $k_R \gtrsim 160$ MeV, the CF has an almost plateaulike appearance, unlike the cases of the $D^0 D^{*-}/D^0 D_s^{*-}$ systems studied in Ref. [37].

It is worth noting that although the CF of a bound state exhibits a "suppression" in the low-momentum region—similar to the behavior observed in systems with repulsive interactions—the underlying physical mechanisms differ significantly. In the bound-state scenario, pairs that form a bound state are lost to the correlation yield, leading to a suppression in the low-momentum region of the CF. In contrast, for the repulsive interaction case, the repulsive force accelerates the particles apart. This increases their relative momentum and similarly suppresses it at low momentum in the CF.

The complete $D_s^+ D_s^-$ CF, incorporating both the strong and Coulomb interactions, is presented in Fig. 5 as a function of the relative momentum k for different source sizes R and for each of the three scenarios. A significant enhancement is observed at the $D_s^+ D_s^-$ threshold in all cases. This effect has been established in various experimental systems, including $p-\Omega$ [58,59] and $p-\Xi$ [59–61] correlations, where the Coulomb interaction plays a significant role at small relative momenta. Our study demonstrates that the $D_s^+ D_s^-$ pair is similarly governed by the Coulomb attraction in the low-k region. Notwithstanding, the low-momentum region retains a distinct and characteristic behavior across interpretations. For small source sizes, the differences are most pronounced: the virtual-state scenario produces a strong enhancement, the bound-state scenario leads to a clear suppression, and the resonant configuration yields a moderate augmentation of the CF, relative to the pure Coulomb CF. This closeness of the resonant CF to the pure Coulomb curve can be understood as follows. While the strong interaction is indeed crucial for forming a resonance, particularly near the resonance energy, its influence near threshold and at low relative momenta is primarily characterized by the scattering length. As shown in Table I, the scattering length for the resonant case has the smallest magnitude (-0.48 in $q_{\max} = 0.5$ GeV and -0.63 in $q_{\max} = 1$ GeV) among the three scenarios, indicating a relatively weak attractive strong interaction. Consequently, the CF for the resonant case remains close to the pure Coulomb result. This interpretation is further supported by Fig. 4, where the resonant CF near threshold is close to unity, reflecting the minimal deviation introduced by the relatively weak strong interaction.

At a relative momentum of $k \approx 100$ MeV, the CF exhibits significant deviations from unity: an enhancement of ∼75% for the virtual state, a smaller enhancement of ∼15% for the resonance, and a suppression of ∼40% for the bound state. These pronounced deviations demonstrate the combined effects of Coulomb and strong interactions. Our results indicate that these distinct patterns persist for smaller values of R, corresponding to smaller collision systems such as pp and pA with light nuclei. Furthermore, they exhibit less sensitivity to the choice of $q_{\max}$, as evidenced in Figs. 4 and 5 for values of 0.5 and 1.0 GeV. This behavior underscores the importance of measuring the $D_s^+D_s^-$ CF in small collision systems, where the contrast between the interpretations is most pronounced.

Hence, the use of femtoscopy to distinguish between a bound, virtual, and resonant state in the $D_s^+D_s^-$ system constitutes the central result of this work, providing a valuable tool to clarify the nature of the $X(3960)$ state.

IV. CONCLUSIONS

In this work, we have given another example of how the combined analysis of line shapes and femtoscopic correlations can help discriminate the underlying structure of exotic hadronic states. In particular, we have investigated the controversy concerning the nature of the $X(3960)$ state, interpreting it as a near-threshold resonance, a virtual state, or a bound $D_s^+D_s^-$ molecule. Using the Bethe-Salpeter formalism to parametrize the strong interaction, our analysis finds that all three scenarios can reproduce the $D_s^+D_s^-$ invariant-mass spectrum of $B^+ \to D_s^+D_s^-K^+$ decays within current experimental uncertainties. After that, by including Coulomb effects in the formalism, we have shown that the $D_s^+D_s^-$ correlation function exhibits distinctive behavior in the low-momentum region, allowing us to distinguish between the three scenarios. Specifically, we predict: a strong enhancement for the virtual-state interpretation, a moderate enhancement for the resonant case, and a clear suppression for the bound-state configuration. These distinct signatures are most pronounced for small source sizes, corresponding possibly to pp and pA collision systems.

Some notes are warranted to discuss the consistency of the findings reported above, particularly regarding coupled-channel effects. As mentioned in the Introduction, a coupled-channel analysis of $D\bar{D}$ and $D_s\bar{D}_s$ systems performed in Ref. [10] found two poles: one below the $D\bar{D}$ threshold and another at 3932.72 MeV with a width of 12.32 MeV, identified as the $X(3930)$. This state couples more strongly to $D_s\bar{D}_s$ than to $D\bar{D}$ and lies closer to the $D_s\bar{D}_s$ threshold than the pole position of our bound-state scenario (Table I). We have checked that the $D_s\bar{D}_s$ CF obtained using the strong scattering amplitude of Ref. [10] does not show qualitative differences with respect to that presented in the previous section for the bound-state configuration.

To conclude, given the recent advances in heavy-flavor femtoscopy, measurements of $D_s^+D_s^-$ correlations in high-multiplicity pp, pA, and AA collisions might be feasible in the near future. They would provide the experimental input needed to shed light on the nature of the $X(3960)$, thereby establishing femtoscopy as a relevant tool in studies of exotic hadrons.

ACKNOWLEDGMENTS

This work is partly supported by the National Key R&D Program of China under Grant No. 2023YFA1606703 and the National Natural Science Foundation of China under Grants No. W2543006 and No. 12435007. L. M. A. is thankful for the hospitality of Beihang University. L. M. A. acknowledges the financial support by the Brazilian CNPq (Grants No. 400215/2022-5, No. 308299/2023-0, No. 402942/2024-8) and CNPq/FAPERJ under the Project INCT-Física Nuclear e Aplicações (Contracts No. 464898/2014-5 and No. 408419/2024-5). Z.-W. L. acknowledges support from the National Natural Science Foundation of China under Grant No. 12405133 and Shenzhen Science and Technology Program under Grant No. ZDSYS20230626091501002.

DATA AVAILABILITY

The data are not publicly available. The data are available from the authors upon reasonable request.

[1] R. Aaij *et al.* (LHCb Collaboration), Phys. Rev. Lett. **131**, 071901 (2023).
[2] R. Aaij *et al.* (LHCb Collaboration), Phys. Rev. Lett. **125**, 242001 (2020).
[3] R. Aaij *et al.* (LHCb Collaboration), Phys. Rev. D **102**, 112003 (2020).
[4] K. Abe *et al.* (Belle Collaboration), Phys. Rev. Lett. **94**, 182002 (2005).
[5] S. Uehara *et al.* (Belle Collaboration), Phys. Rev. Lett. **104**, 092001 (2010).
[6] B. Aubert *et al.* (*BABAR* Collaboration), Phys. Rev. Lett. **101**, 082001 (2008).
[7] J. P. Lees *et al.* (*BABAR* Collaboration), Phys. Rev. D **86**, 072002 (2012).
[8] T. Barnes, S. Godfrey, and E. S. Swanson, Phys. Rev. D **72**, 054026 (2005).

[9] B.-Q. Li and K.-T. Chao, Phys. Rev. D **79**, 094004 (2009).
[10] M. Bayar, A. Feijoo, and E. Oset, Phys. Rev. D **107**, 034007 (2023).
[11] T. Ji, X.-K. Dong, M. Albaladejo, M.-L. Du, F.-K. Guo, and J. Nieves, Phys. Rev. D **106**, 094002 (2022).
[12] T. Ji, X.-K. Dong, M. Albaladejo, M.-L. Du, F.-K. Guo, J. Nieves, and B.-S. Zou, Sci. Bull. **68**, 688 (2023).
[13] L. M. Abreu, M. Albaladejo, A. Feijoo, E. Oset, and J. Nieves, Eur. Phys. J. C **83**, 309 (2023).
[14] D. Gamermann, E. Oset, D. Strottman, and M. J. Vicente Vacas, Phys. Rev. D **76**, 074016 (2007).
[15] J. Nieves and M. P. Valderrama, Phys. Rev. D **86**, 056004 (2012).
[16] C. Hidalgo-Duque, J. Nieves, and M. P. Valderrama, Phys. Rev. D **87**, 076006 (2013).
[17] S. Prelovsek, S. Collins, D. Mohler, M. Padmanath, and S. Piemonte, J. High Energy Phys. 06 (2021) 035.
[18] P. C. S. Brandão, J. Song, L. M. Abreu, and E. Oset, Phys. Rev. D **108**, 054004 (2023).
[19] L. M. Abreu and J. M. Torres-Rincon, Phys. Rev. D **112**, 016003 (2025).
[20] D. J. Wilson, C. E. Thomas, J. J. Dudek, and R. G. Edwards (Hadron Spectrum Collaboration), Phys. Rev. Lett. **132**, 241901 (2024).
[21] Q. Xin, Z.-G. Wang, and X.-S. Yang, AAPPS Bull. **32**, 37 (2022).
[22] H. Mutuk, Eur. Phys. J. C **82**, 1142 (2022).
[23] R. Chen and Q. Huang, Phys. Lett. B **846**, 138254 (2023).
[24] S. S. Agaev, K. Azizi, and H. Sundu, Phys. Rev. D **107**, 054017 (2023).
[25] T. Guo, J. Li, J. Zhao, and L. He, Chin. Phys. C **47**, 063107 (2023).
[26] A. M. Badalian and Y. A. Simonov, Eur. Phys. J. C **83**, 410 (2023).
[27] J.-M. Xie, M.-Z. Liu, and L.-S. Geng, Phys. Rev. D **107**, 016003 (2023).
[28] M. A. Lisa, S. Pratt, R. Soltz, and U. Wiedemann, Annu. Rev. Nucl. Part. Sci. **55**, 357 (2005).
[29] S. Acharya *et al.* (ALICE Collaboration), Phys. Rev. Lett. **127**, 172301 (2021).
[30] M.-Z. Liu, Y.-W. Pan, Z.-W. Liu, T.-W. Wu, J.-X. Lu, and L.-S. Geng, Phys. Rep. **1108**, 1 (2025).
[31] Z.-W. Liu, J.-X. Lu, and L.-S. Geng, Proc. Sci. QNP2024 (**2025**) 044.
[32] E. Chizzali, Y. Kamiya, R. Del Grande, T. Doi, L. Fabbietti, T. Hatsuda, and Y. Lyu, Phys. Lett. B **848**, 138358 (2024).
[33] Z.-W. Liu, K.-W. Li, and L.-S. Geng, Chin. Phys. C **47**, 024108 (2023).
[34] Z.-W. Liu, J.-X. Lu, and L.-S. Geng, Phys. Rev. D **107**, 074019 (2023).
[35] Z.-W. Liu, J.-X. Lu, M.-Z. Liu, and L.-S. Geng, Phys. Rev. D **108**, L031503 (2023).
[36] R. Molina, Z.-W. Liu, L.-S. Geng, and E. Oset, Eur. Phys. J. C **84**, 328 (2024).
[37] Z.-W. Liu, J.-X. Lu, M.-Z. Liu, and L.-S. Geng, Sci. Bull. **70**, 3515 (2025).
[38] A. Feijoo, M. Korwieser, and L. Fabbietti, Phys. Rev. D **111**, 014009 (2025).
[39] L. M. Abreu, P. Gubler, K. P. Khemchandani, A. Martinez Torres, and A. Hosaka, Phys. Lett. B **860**, 139175 (2025).
[40] Z.-W. Liu, D.-L. Ge, J.-X. Lu, M.-Z. Liu, and L.-S. Geng, Phys. Rev. D **112**, 054019 (2025).
[41] Y.-b. Shen, Z.-W. Liu, J.-X. Lu, M.-Z. Liu, and L.-S. Geng, arXiv:2506.23476.
[42] J.-M. Xie, Z.-W. Liu, J.-X. Lu, H. Liang, R. Molina, and L.-S. Geng, Phys. Rev. D **113**, 074002 (2026).
[43] S. Acharya *et al.* (ALICE Collaboration), Phys. Rev. D **106**, 052010 (2022).
[44] S. Acharya *et al.* (ALICE Collaboration), Phys. Rev. D **110**, 032004 (2024).
[45] A. Feijoo, L. R. Dai, L. M. Abreu, and E. Oset, Phys. Rev. D **109**, 016014 (2024).
[46] L. R. Dai, L. M. Abreu, A. Feijoo, and E. Oset, Eur. Phys. J. C **83**, 983 (2023).
[47] K. P. Khemchandani, L. M. Abreu, A. Martinez Torres, and F. S. Navarra, Phys. Rev. D **110**, 036008 (2024).
[48] Y.-B. Shen, M.-Z. Liu, Z.-W. Liu, and L.-S. Geng, Phys. Rev. D **111**, 034001 (2025).
[49] L. Fabbietti, V. Mantovani Sarti, and O. Vazquez Doce, Annu. Rev. Nucl. Part. Sci. **71**, 377 (2021).
[50] S. E. Koonin, Phys. Lett. **70B**, 43 (1977).
[51] S. Pratt, Phys. Rev. D **33**, 1314 (1986).
[52] D.-L. Ge, Z.-W. Liu, J.-X. Lu, and L.-S. Geng, Phys. Rev. C **112**, 034003 (2025).
[53] P. Encarnación, A. Feijoo, V. M. Sarti, and A. Ramos, Phys. Rev. D **111**, 114013 (2025).
[54] C. J. Joachain, *Quantum Collision Theory* (North-Holland Publishing Company, Amsterdam, 1975).
[55] I. Vidana, A. Feijoo, M. Albaladejo, J. Nieves, and E. Oset, Phys. Lett. B **846**, 138201 (2023).
[56] M. Albaladejo, J. Nieves, and E. Ruiz-Arriola, Phys. Rev. D **108**, 014020 (2023).
[57] J. M. Torres-Rincon, A. Ramos, and L. Tolos, Phys. Rev. D **108**, 096008 (2023).
[58] J. Adam *et al.* (STAR Collaboration), Phys. Lett. B **790**, 490 (2019).
[59] A. Collaboration *et al.* (ALICE Collaboration), Nature (London) **588**, 232 (2020); **590**, E13(E) (2021).
[60] M. Isshiki (STAR Collaboration), EPJ Web Conf. **259**, 11015 (2022).
[61] S. Acharya *et al.* (ALICE Collaboration), Phys. Rev. Lett. **123**, 112002 (2019).